# Equation of state, phase transitions, and band-gap closure in $PbCl_2$ and $SnCl_2$

T. J. Smart,[1] E. F. O'Bannon, III,[2] M. R. Diamond,[1] S. Stackhouse,[3] B. K. Godwal,[1] Q. Williams,[4] and R. Jeanloz[1]
[1]*Department of Earth and Planetary Science, University of California, Berkeley, California, 94720–4767, USA*
[2]*Physics Division, Physical & Life Sciences Directorate, Lawrence Livermore National Laboratory, Livermore, California 94551, USA*
[3]*School of Earth and Environment, University of Leeds, LS2 9JT, United Kingdom*
[4]*Department of Earth and Planetary Sciences, University of California, Santa Cruz, California 95064, USA*

(Received 8 September 2020; revised 20 April 2022; accepted 29 November 2022; published 20 April 2023)

The equations of state and band-gap closures for $PbCl_2$ and $SnCl_2$ were studied using both experimental and theoretical methods. We measured the volume of both materials to a maximum pressure of 70 GPa using synchrotron-based angle-dispersive powder x-ray diffraction. The lattice parameters for both compounds showed anomalous changes between 16–32 GPa, providing evidence of a phase transition from the cotunnite structure to the related $Co_2Si$ structure, in contrast to the postcotunnite structure as previously suggested. First-principles calculations confirm this finding and predict a second phase transition to a $Co_2Si$-like structure between 75–110 GPa in $PbCl_2$ and 60–75 GPa in $SnCl_2$. Band gaps were measured under compression to ∼70 GPa for $PbCl_2$ and ∼66 GPa for $SnCl_2$ and calculated up to 200 GPa for $PbCl_2$ and 120 GPa for $SnCl_2$. We find an excellent agreement between our experimental and theoretical results when using the Heyd-Scuseria-Ernzerhof (HSE06) hybrid functional, which suggests that this functional could reliably be used to calculate the band gap of similar $AX_2$ compounds. Experimental and calculated band-gap results show discontinuous decreases in the band gap corresponding to phase changes to higher-coordinated crystal structures, giving insight into the relationship between interatomic geometry and metallicity.

DOI: 10.1103/PhysRevB.107.134113

## I. INTRODUCTION

Understanding the relationship between atomic structure and electronic properties at high pressure is a long-standing pursuit in the fields of condensed-matter and high energy-density physics, as well as in planetary and materials sciences, with the discovery of materials having technologically important properties (e.g., ferroelectrics, superconductors) being among the motivations [1–3]. Compression can transform materials to the metallic state by way of both classical (electrostatic repulsion) and quantum (Pauli exclusion) effects favoring delocalized electron states with increased density [4,5]. However, it is unclear how changing local atomic-packing structure (e.g., coordination number) affects metallicity, as a material transforms to more highly coordinated structures under compression. Nevertheless, we recognize that most simple metals crystallize in close-packed structures (coordination number = 12) at ambient conditions [6].

Numerous studies of insulator-to-metal transitions under pressure have focused on the $AX_2$ family of compounds, which draw interest from a range of fields due to their planetary and technological importance and diversity in bonding character (e.g., halides, oxides, intermetallic) [7–19]. Of particular interest is $SiO_2$, the archetypical rock-forming compound, whose presence is expected in the deep interiors of giant ($H_2$ + He), "icy" (molecular species, along with $H_2$ and He), and large-terrestrial (e.g., "super-Earth") planets [12,14,20].

The highest-pressure observations of $AX_2$ compounds ($SiO_2$, $CaF_2$) document the insulator-to-metal transition under dynamic compression, in which elevated temperatures melt the sample prior to metallization [20,21]. Notably, in at least some of these compounds (e.g., $SiO_2$, $AuGa_2$), nearest-neighbor coordination increases under compression while in the fluid state, follows the trend displayed in solid-state structures on compression [22–24]. However, the short timescales and fluid samples of these make typical methods of quantifying the interatomic geometry (e.g., x-ray diffraction) challenging, motivating the study of analog compounds that already have highly coordinated cations at ambient conditions to document the relationship between band-gap closure and interatomic geometry.

$AX_2$ compounds, despite their diversity in bonding character, typically follow a sequence of predictable structural transitions on compression, with cation coordination increasing at each step (Fig. 1) [7–19]. This sequence is considered well established up to the ninefold-coordinated cotunnite phase. High-pressure studies of $AX_2$ compounds that crystallize in the cotunnite phase at ambient conditions (e.g., $PbCl_2$ and $SnCl_2$) thus allow us to extend our understanding of the role of interatomic geometry on electronic and other material properties beyond the established regime.

In this study, we characterize the crystal structures, equations of state, and band gaps of $PbCl_2$ and $SnCl_2$ to pressures of over 70 GPa and compare our measurements with the results of *ab initio* electronic structure calculations. Given that metallization (e.g., band-gap closure) is notoriously challenging to predict using first-principles calculations, experiments can be used to check theory, which—-to the degree that it is thereby validated—-can provide fruitful predictions of material properties at pressure-temperature conditions

 

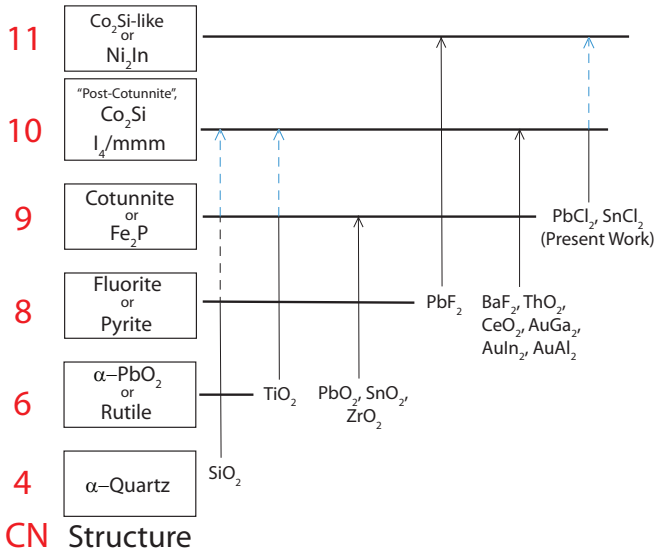


FIG. 1. Crystal-structural sequence of $AX_2$ compounds at ambient conditions and high pressures. Figure after Leger *et al.* [4]. Cation coordination number (CN) of the cation is shown on the left, next to the structure name. Several $AX_2$ compounds are shown with arrows noting experimentally determined high-pressure phases [7–19]. Dashed arrows denote structures calculated from first principles, and blue color indicates that metallization is expected for the high-pressure phase. Several compounds (e.g., $GeO_2$, $Na_2Te$, $HgF_2$, $BaCl_2$, $BaI_2$, $BaBr_2$), and the effects of temperature are omitted for clarity.

that are not accessible with current experimental techniques [25,26].

## II. METHODS

### A. High-pressure experiments

Polycrystalline $PbCl_2$ and $SnCl_2$ (Sigma-Aldrich >99% purity, with natural isotopic ratios) were ground to micrometer-sized grains and loaded into symmetric-type diamond-anvil cells, leaving ∼30% void space to allow room for the pressure medium. Diamond anvils had a culet size of 200 μm, and rhenium gaskets preindented to ∼30-μm thickness and drilled with 80-μm diameter holes were used. Ruby spheres of ⩽5-μm diameter were placed inside the sample chamber and ruby fluorescence was used to determine the pressure [27].

All experiments were conducted at room temperature: this is substantially above the Debye temperatures of these materials, as estimated from their ambient-pressure vibrational spectra [28,29], and hence the presence of different isotopes is not expected to affect their high-pressure transitions at room temperature.

Samples were loaded in either a neon pressure medium, or a 16:3:1 methanol:ethanol:water pressure medium. $SnCl_2$ is hygroscopic, so it was loaded in a dry argon atmosphere. Midinfrared spectra were collected to affirm minimal water content of $SnCl_2$ samples before all high-pressure experiments.

The band gap (absorption edge) was measured through visible and near-infrared spectroscopy. In all experiments a background measurement was collected using a fully assembled but empty diamond cell and the background was subtracted from the spectra. Optical absorption spectra were collected on a Horiba LabRam HR Evolution Raman spectrometer, with a white light source being used to collect spectra from 400–800 nm (3.1–1.55 eV). Near-infrared spectra were collected using an evacuated Bruker Vertex 70v FTIR equipped with a tungsten source, InSb detector, and $CaF_2$ beam splitter [30]. Spectra were collected from 14 000 to 8500 $cm^{-1}$ (714.3 to 1176.5 nm, 1.74 to 1.05 eV) with a resolution of 4 $cm^{-1}$ (0.2–0.6 nm across this frequency range). As a note, though the sensor resolution is on the meV scale, we observe band-gap closure in our samples on the scale of eV over tens of GPa, indicating that the true resolution of absorption-edge measurements is controlled by the resolution of our pressure measurements and is on the scale of ∼0.1 eV. No pressure medium was used in the experiments to measure the band gap under pressure, and the pressure gradients in these experiments are large. However, because of the spatial resolution of our instrument and the sharpness of the absorption edge of our samples, we do not anticipate that nonhydrostatic conditions adversely affect our band-gap determinations.

Angular-dispersive synchrotron x-ray diffraction experiments were performed at beamline 12.2.2 at the Advanced Light Source (Lawrence Berkeley National Laboratory), using a monochromatic x-ray beam with $\lambda = 0.4959$ Å (25 keV). A Mar345 detector collected diffracted x rays at 331.4 (±0.1) mm. Detector distance and orientation were calibrated using a $LaB_6$ standard, and the diffraction images were radially integrated using the programs FIT2D [31] or DIOPTAS [32].

We carried out Rietveld refinements using the General Structure Analysis System (GSAS) [33] LARSON program, with starting atom positions chosen from the outputs of *ab initio* density-functional theory described in the following section. After fitting the background, the data were refined for lattice parameters. Pseudo-Voigt functions are used for the fitting of diffraction-peak profiles in the Rietveld refinements.

### B. Theoretical calculations

All calculations were performed using the density-functional theory-based Vienna *Ab initio* Simulation Package VASP code, employing the projector augmented-wave method [33–37]. The potentials were generated using valence configurations of $4d^{10}\ 5s^2\ 5p^2$ for Sn, $5d^{10}\ 6s^2\ 6p^2$ for Pb, and $3s^2\ 3p^5$ for Cl. Scalar relativistic effects were accounted for. However, spin-orbit coupling was only included in the calculations for $PbCl_2$ phases because it was found to have a negligible effect on the results of calculations for $SnCl_2$ phases. Computations were performed using both the local-density approximation (LDA) and Perdew-Burke-Ernzerhof (PBE) formulation of the generalized gradient approximation (GGA) [38,39]. The LDA and GGA give reasonable estimates of structural parameters, but underestimate band gaps (e.g., Xiao *et al.*, 2011) [40], due to their inherently incomplete cancellation of self-interaction [25,26]. In view

of this, additional band-gap calculations were performed using the Heyd-Scuseria-Ernzerhof (HSE06) hybrid functional, which incorporates a fraction of exact exchange to alleviate the self-interaction error, on structures optimized using the PBE functional [41]. The HSE06 hybrid functional predicts band gaps that are in much better agreement with experimental measurements, but has a high computational cost, making it unsuitable for geometry optimizations in the present work [40,42]. HSE06 was chosen out of the popular hybrid density functionals, because it is shown to be the most accurate in calculating the band gaps of semiconductors [42].

For geometry optimization calculations, the kinetic-energy cutoff for the plane-wave expansion was 600 eV, and Brillouin-zone sampling was performed using a $6 \times 4 \times 8$ $k$-point grid [43]. These settings ensured calculated volumes were converged to within 0.05 $Å^3$, and enthalpies to within 1 meV per atom.

For LDA and PBE band-gap calculations, the kinetic-energy cutoff for the plane-wave expansion was 600 eV, and Brillouin-zone sampling was performed using an $11 \times 7 \times 15$ $k$-point grid [43]. These settings ensured that calculated band gaps were converged to within about 0.05 eV or less. Due to the high computational cost associated with hybrid functional calculations, for HSE06 band-gap and density of states calculations, Brillouin-zone sampling was performed using a $5 \times 3 \times 7$ $k$-point grid [43]. Convergence tests for LDA and PBE suggest that using this smaller $k$-point grid leads to overestimates of the band gap of up to 0.05 eV for $SnCl_2$ and 0.2 eV for $PbCl_2$.

It is well known that LDA underestimates pressure, and PBE overestimates pressure. Because of this, a pressure correction was estimated using the method of Oganov *et al.* [44], but without a thermal pressure term (this is likely negligible at ambient temperature for these calculations performed at 0 K). The calculated pressure shifts [$PbCl_2$: +2 GPa (LDA), −2 GPa (PBE); $SnCl_2$: +2 GPa (LDA), −1 GPa (PBE)] move the isothermal compression curves to higher or lower pressure, bringing them in better accord with experimental values.

## III. RESULTS AND DISCUSSION

### A. X-ray diffraction results

X-ray diffraction data were collected on compression and decompression to 71 GPa in both $PbCl_2$ and $SnCl_2$ (Fig. 2; example diffraction patterns shown in Appendix A, Figs. 6 and 7). Rietveld refinements of the diffraction patterns for both compounds document an isosymmetric phase transition from the cotunnite structure (orthorhombic *Pnma*, ninefold coordination) to the $Co_2Si$ structure (orthorhombic *Pnma*, tenfold coordination) between 17 and 35 GPa for $PbCl_2$ and 17 to 33 GPa for $SnCl_2$, supporting a prior theoretical prediction [45] (see Fig. 4 for structural diagrams). These findings are consistent with structural transitions documented in other $AX_2$ compounds such as $PbF_2$, $BaCl_2$, and $BaBr_2$ [9,13], and the gradual nature of the transition is fully compatible with the close topological relationship between the cotunnite structure and the $Co_2Si$ structure [46].

Measured lattice parameters provide a greater insight into the structural transition that occurs over a relatively large pressure range for both materials. The cotunnite-to-$Co_2Si$ transition in these materials is characterized by an anomalous shift in relative length of lattice parameters (Fig. 3) [47]. This occurs between 17 and 35 GPa for $PbCl_2$ and between 17 and 33 GPa for $SnCl_2$. In these regions we observe anisotropic compressibility of the unit cell, with a strong compression along the $a$ axis, a reduced compression along $c$-, and extension along $b$-, which has been reported to occur in other $AX_2$ compounds that transform from the cotunnite structure to the $Co_2Si$ structure under compression (e.g., $PbF_2$, $CeO_2$, and $ThO_2$) [13,18]. While we were not able to collect data on decompression in the pressure range of this phase transition in $SnCl_2$, in $PbCl_2$ the transition is observed to be reversible with minor hysteresis.

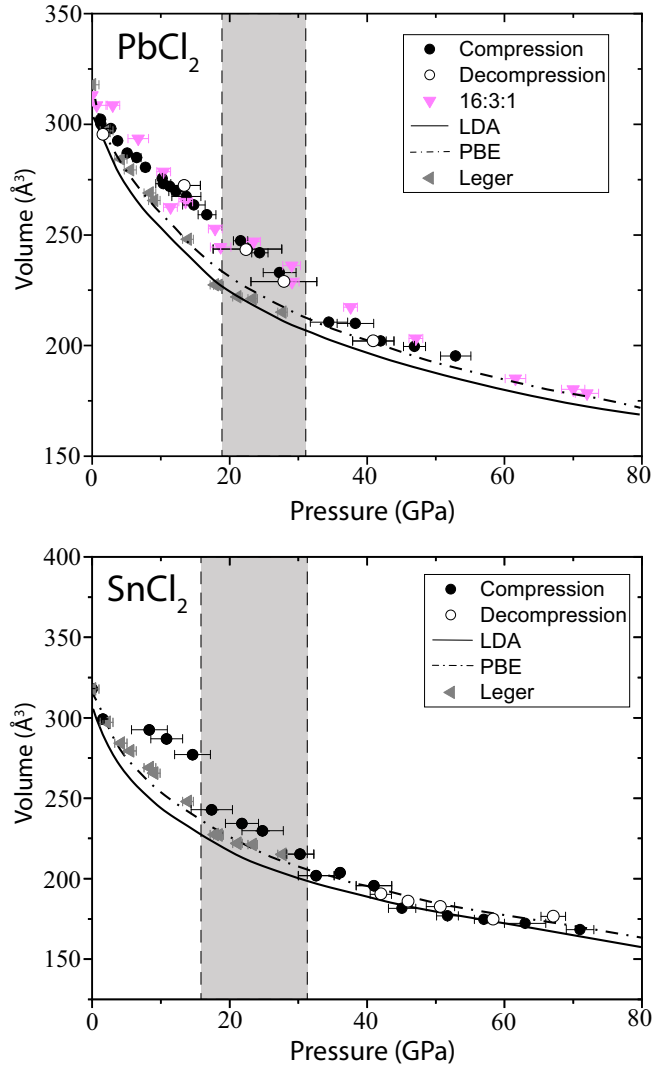


FIG. 2. Pressure-volume data for $PbCl_2$ (top) and $SnCl_2$ (bottom). Data shown in black or hollow circles were taken using neon pressure medium. Pink triangles not data taken using 16:3:1 methanol:ethanol:water pressure medium, and gray triangle*s* are previous results from Leger *et al.* [10].The pressure range for the transformation from cotunnite to $Co_2Si$ structures, between 17 and 35 GPa for $PbCl_2$ and 17 and 33 GPa for $SnCl_2$, is shown by the gray box between dashed lines as it is for Figs. 3 and 8 . Data collected on compression and decompression are distinguished by closed and open circles, respectively.

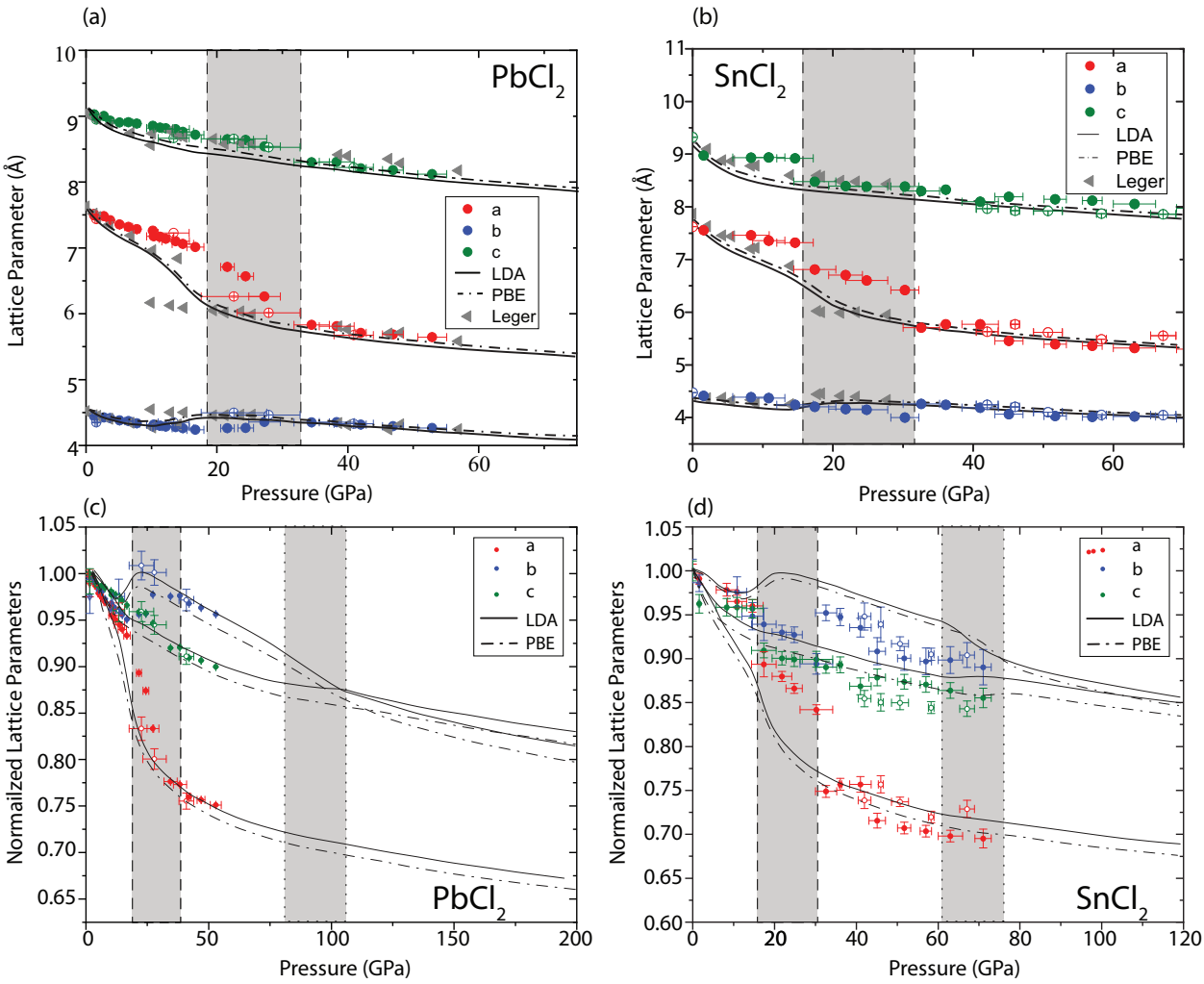


FIG. 3. Lattice parameters vs pressure from experiments and theory are presented for $PbCl_2$ (a) and $SnCl_2$ (b). Lattice parameters normalized against ambient-pressure values are presented as a function of pressure for $PbCl_2$ (c) and $SnCl_2$ (d). Lattice parameters show a gradual change in slope between 21 and 25 GPa for $PbCl_2$ and between 17 and 33 GPa for $SnCl_2$, contrasting with previous work that showed a sharp transition [gray triangles in (a) and (b)]. We infer a gradual change in phase ("transition zone"), consistent with findings for other $AX_2$ compounds as the materials shift from the cotunnite to $Co_2Si$ structure. We mark these transition zones with gray boxes, whose boundaries are defined by the observed shifts in lattice parameters (gray boxes with dashed black lines). The experimentally observed compression of the *a* and *c* axes and extension of the *b* axis is reflected in calculations. Upon further compression, LDA and PBE calculations predict a distortion of the $Co_2Si$ lattice, seen here as a slight contraction of the *b* axis and extension of the *c* axis between 75 and 110 GPa in $PbCl_2$ and between 60 and 75 GPa in $SnCl_2$, shown by the gray box between dotted lines in (c) and (d).

The strong compression of the *a* axis relative to the *b*- and *c* axes is emphasized when we normalize the lattice parameters against their respective initial lengths [Figs. 3(c) and 3(d)]. The pressure range of the phase transition is marked by the gray shading between dashed lines, with a smooth transition in $PbCl_2$ that is complete by 33 GPa, and a sudden shift in $SnCl_2$ at 33 GPa. Due to the non-negligible pressure gradients, we attribute this more sudden shift between phases to be a result of nonhydrostatic stresses.

Previous experiments by Leger *et al.* [10] did not exhibit these continuous trends in lattice parameters or the presence of an intermediate phase and had strong hysteresis on decompression (gray triangles, Figs. 2 and 3). This difference is likely associated with the more nonhydrostatic stress environments within the samples of their experiments, as these had no pressure medium for $SnCl_2$ and silicone grease for $PbCl_2$. Because of the contrast in the nature of the transition (abrupt in the previous experiments and with an intermediate zone of transformation in ours), we do not preclude that the transition from the cotunnite to the $Co_2Si$ structure can be driven (enhanced) by nonhydrostatic stresses.

Density-functional theory calculations agree well with experimental data, with compression of the *a* axis and extension of the *b* axis reproduced by the calculations, albeit at pressures ∼10 GPa lower than experimentally observed (Figs. 2 and 3). Between 75 and 110 GPa in $PbCl_2$ and 60 and 75 GPa in $SnCl_2$, PBE and LDA functionals predict another shift in structure from the tenfold-coordinated $Co_2Si$ structure to an 11-fold–coordinated $Co_2Si$-like phase (structure shown in Fig. 4). This phase shares the same space group as the $Co_2Si$

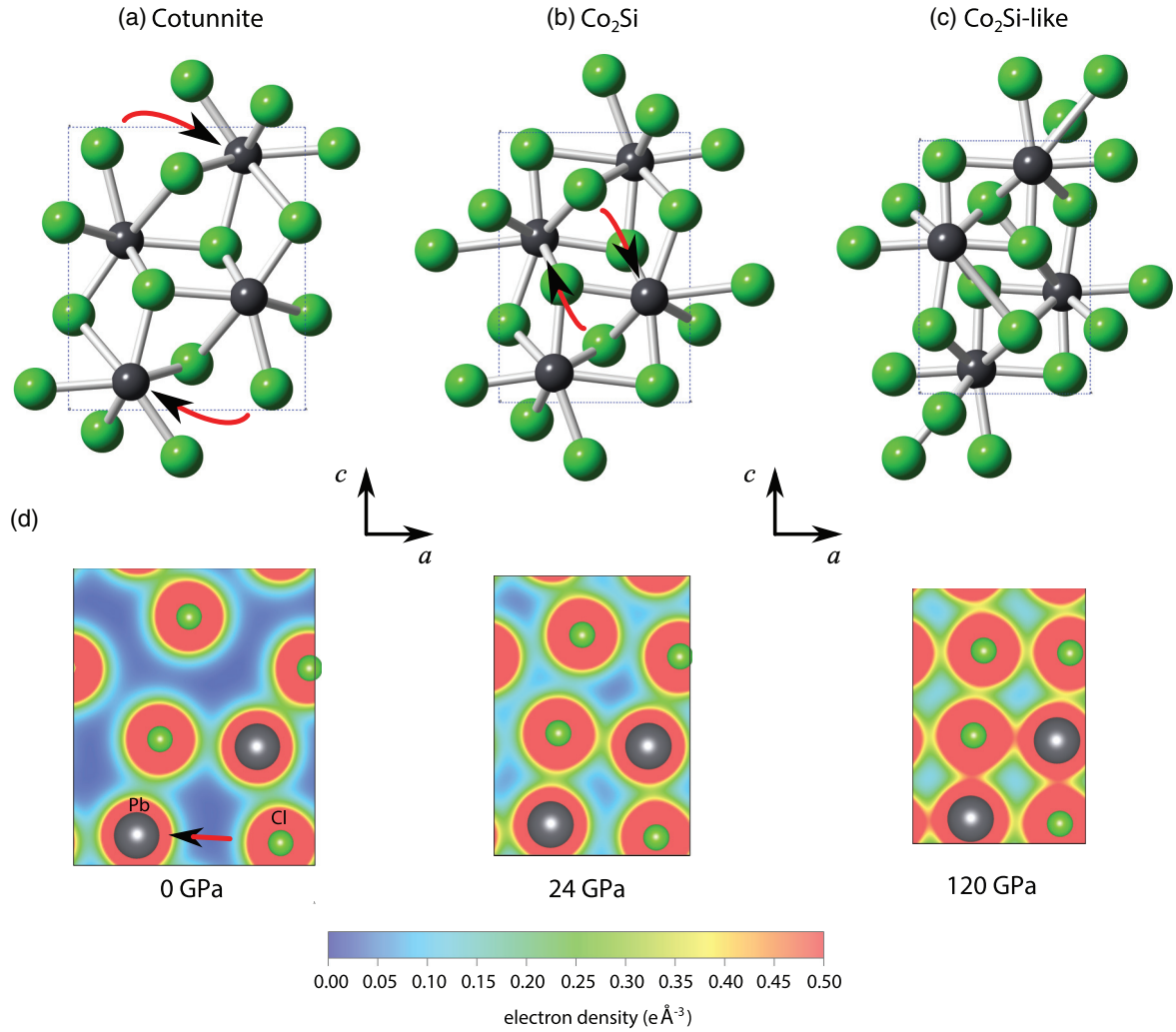


FIG. 4. Structural diagrams of the cotunnite, $Co_2Si$, and $Co_2Si$-to-$Co_2Si$-like phases, with the Pb, Sn cations shown in black and chlorine shown in green. (a)–(c) show ball-and-stick models of the cotunnite, $Co_2Si$, and $Co_2Si$-like structures, respectively, with arrows indicating the atomic motion that leads to bonds in subsequent phases. (d) Change in electron density in the (010) plane as a function of pressure. A bond forms between Pb and Cl at 24 GPa, indicative of a transformation from the ninefold-coordinated cotunnite structure (a) to the tenfold-coordinated $Co_2Si$ structure (b). For $SnCl_2$, formation of an analogous Sn-Cl bond is observed at about 28 GPa. On further compression the lattice continues to become more ideally packed, and (Pb,Sn)-Cl bonds form. This $Co_2Si$-like structure is predicted by DFT to occur at 120 GPa in $PbCl_2$ and 80 GPa in $SnCl_2$. Figures were produced using VESTA3 [50].

structure (*Pnma*), but the rows of atoms become increasingly collinear and orthogonal to one another, as the anion sublattice begins to approach a close-packed array. The transition is characterized by a subtle extension of the *c* axis and compression of the *b* axis, which has pronounced expression in the normalized lattice parameters plots [Figs. 3(c) and 3(d), gray shading between dotted lines]. As has been previously noted [12], the ninefold cation coordination of the cotunnite structure is incompatible with close packing of the anion framework. Indeed, the cotunnite structure can be viewed as comprising interlinked $(MX_2)_n$ polymeric chains [48]. The sequential transitions can then be viewed as a progression from a phase characterized by high cation coordination but an inefficiently packed anion sublattice (anions coordinated in trigonal prisms) to a phase with both higher-cation coordination and far more efficiently packed anions [Fig. 4(d)]. The transition sequence is a higher-coordination analog to the structural shifts in the $SiO_2$-system at lower pressures, in which a polymeric low-pressure phase (quartz, with corner-linked $SiO_4$ tetrahedra) converts to the close-packed and more highly coordinated rutile structure.

Structural rearrangements from the cotunnite to $Co_2Si$ and then to $Co_2Si$-like phases are shown in Fig. 4; the formation of bonds between Pb or Sn and Cl is indicated by the red and black arrows. Electron density maps [Fig. 4(d)] show that formation of the first bond (shown by the red and black arrow) occurs at 24 GPa in $PbCl_2$ and at 28 GPa in $SnCl_2$ (not shown), similar pressures to observations of analogous bonds forming in $PbF_2$ by Stan *et al.* [13]. Further compression leads to a tightly packed arrangement, with atoms forming an increasingly square lattice within each layer in the (010) plane, until the structure becomes 11-fold–coordinated ($Co_2Si$-like structure) at 110 GPa in $PbCl_2$ and at 75 GPa in $SnCl_2$.

TABLE I. Comparison of our equations of state with previous work by Leger *et al.* [10]. Zero-pressure volume $V_0$, bulk modulus $K_0$, and pressure derivative $K_0'$ for the high-pressure phases ($Co_2Si$ and $Co_2Si$-like) are determined through third-order Birch-Murnaghan equations of state by fitting normalized pressure to Eulerian strain ($G$ vs $g$) [49] (see Appendix B, Fig. 8 for details). The volume $V_0$ for the ambient pressure cotunnite phase is obtained from our x-ray diffraction data via Rietveld refinement and are fixed in these fits. Equations of state for the $Co_2Si$-like structure are determined from outputs from PBE calculations. Bold lettering indicates values that were fixed in our fits.

| | Cotunnite structure | | | $Co_2Si$ structure | | | $Co_2Si$-like structure | | |
|---|---|---|---|---|---|---|---|---|---|
| Reference | $\mathbf{V_0}$ | $\mathbf{K_0}$ | $\mathbf{K'_0}$ | $\mathbf{V_0}$ | $\mathbf{K_0}$ | $\mathbf{K'_0}$ | $\mathbf{V_0}$ | $\mathbf{K_0}$ | $\mathbf{K'_0}$ |
| $PbCl_2$ This study | **313.06 ± 0.05** | 46.7 ± 4.4 | 4.8 ± 1.2 | 300(20) | 47.2 ± 3.2 | 4.0 ± 1.0 | 286(3) | 59.2 ± 0.3 | 4.0 ± 0 |
| $SnCl_2$ This study | **318.03 ± 0.05** | 27.9 ± 2.1 | 6.3 ± 0.5 | 292(43) | 41.1 ± 3.7 | 4.0 ± 0.2 | 290(8) | 43.7 ± 0.1 | 4.0 ± 0 |
| $PbCl_2$ Ref. [10] | 313.072 | 34 ± 1 | 7.4 ± 6 | 273.91 | 95 ± 10 | 4.3 ± 5 | | | |
| $SnCl_2$ Ref. [10] | 317.853 | 31 ± 2 | 4.9 ± 8 | 263.81 | 91 ± 10 | **4.0** | | | |

We fit our pressure-volume data with a third-order Birch-Murnaghan equation of state (EOS), and the obtained parameters are shown in Table I. EOSs previously reported [10] were determined assuming a single phase, and we obtain similar results when we fit our data in this way. However, when we fit our high- and low-pressure phases separately, we find the high-pressure phase to have higher $V_0$ and lower bulk modulus $K_0$ than previously reported (fits shown in Appendix B, Fig. 8).

### B. Band-gap measurements

Representative absorption-edge spectra, collected between 30 and 70 GPa for $PbCl_2$ and between 20 and 66 GPa for $SnCl_2$, show good agreement with theory (Fig. 5 and Appendix D; see Fig. 10 and Table II). Of the three functionals used, as expected HSE06 agrees best with the experimental data, overestimating the band gap by only 0.2 eV, which is due to an incomplete convergence with respect to k-point sampling.

For $PbCl_2$ and $SnCl_2$ we observe three distinct regions in the theoretically calculated band gaps with compression. Discontinuities in the band gap vs volume plots, and shallowing slope in the band gap vs volume plots are attributed to changes in $PbCl_2$ and $SnCl_2$ as they transform from the cotunnite to $Co_2Si$ phase (gray box with dashed lines) and from the $Co_2Si$ to $Co_2Si$-like phase (gray boxes with dotted lines). Experimental data for $SnCl_2$ follow this trend, closely following values calculated by the HSE06 functional, at pressures and volumes coinciding with the calculated structural changes [Fig. 5(b) and 5(d)].

When the experimental $PbCl_2$ data are extrapolated to zero band gap, we predict band closure at 206 ± 24 GPa, which agrees with HSE06 calculated band-gap closure at 200 GPa. When we extrapolate the experimental $SnCl_2$ data for the $Co_2Si$-like phase (between 51 and 66 GPa) to zero band gap, we predict band closure at 125 ± 9 GPa versus 120 GPa predicted by HSE06. If, however, we extrapolate the entire $SnCl_2$ experimental dataset to zero band gap, we predict band closure at 97 ± 6 GPa, representing a 20-GPa discrepancy between experiments and HSE06.

The lower metallization pressure of $SnCl_2$ relative to $PbCl_2$ differs from the typical trend of metallization pressures decreasing along isoelectronic series down the periodic table to heavier, more electron-rich compounds. This trend, which is also found in band-structure calculations of other compounds [51,52], does not predict the relative band-gap closure pressures of the two compounds examined here. This apparent inversion of metallization pressure is likely generated by the relativistic down-shift and associated localization of the 6*s* lone pair in Pb relative to the somewhat more delocalized 5*s* lone pair in Sn. Indeed, portions of the Pb 6*s* states are among the deepest in the valence band at all pressures, and the 5*s* states of Sn systematically contribute substantially more to the density of states at the top of the valence band relative to the 6*s* states in $PbCl_2$ (see Appendix E, Fig. 11). Comparable lowering of the band gap of SnO relative to PbO via this "inert lone pair" has been extensively documented at ambient pressures [53,54], and we demonstrate here that this 6*s* localization persists to high pressures in the chlorides of these elements.

We observe a dramatic increase in slope in the band gap vs volume plot at high compression (Fig. 5, bottom panels). During compression of the initial cotunnite phase in both compounds, we observe a small reduction in band energy predicted by HSE06 calculations (5 and 14% of ambient pressure band gap for $PbCl_2$ and $SnCl_2$, respectively), despite a significant change in unit-cell volume (roughly 50% of the total volume closure of the materials, with total volume closure $V_{tot} = V_0 - V_{band\ closure}$). At the onset of the transition between ninefold-coordinated cotunnite and tenfold-coordinated $Co_2Si$ structures, we observe a large (>20%) reduction in the band gap in both compounds, despite small reductions in unit-cell volume (∼14% of $V_{tot}$). This transition is also accompanied by a shift in the cation coordination around the anions, from 4 and 5 for the two different Cl sites in the cotunnite structure toward 5 and 6 in the $Co_2Si$ structure (as illustrated by the Pb-Cl bond formation in Fig. 4). Upon further compression in the $Co_2Si$ region, the slope becomes steeper, with small changes in the unit-cell volumes (∼3% $V_{tot}$) producing large decreases in the band gap. We find a significant drop in band gap at the expected $Co_2Si$-to-$Co_2Si$-like phase boundary

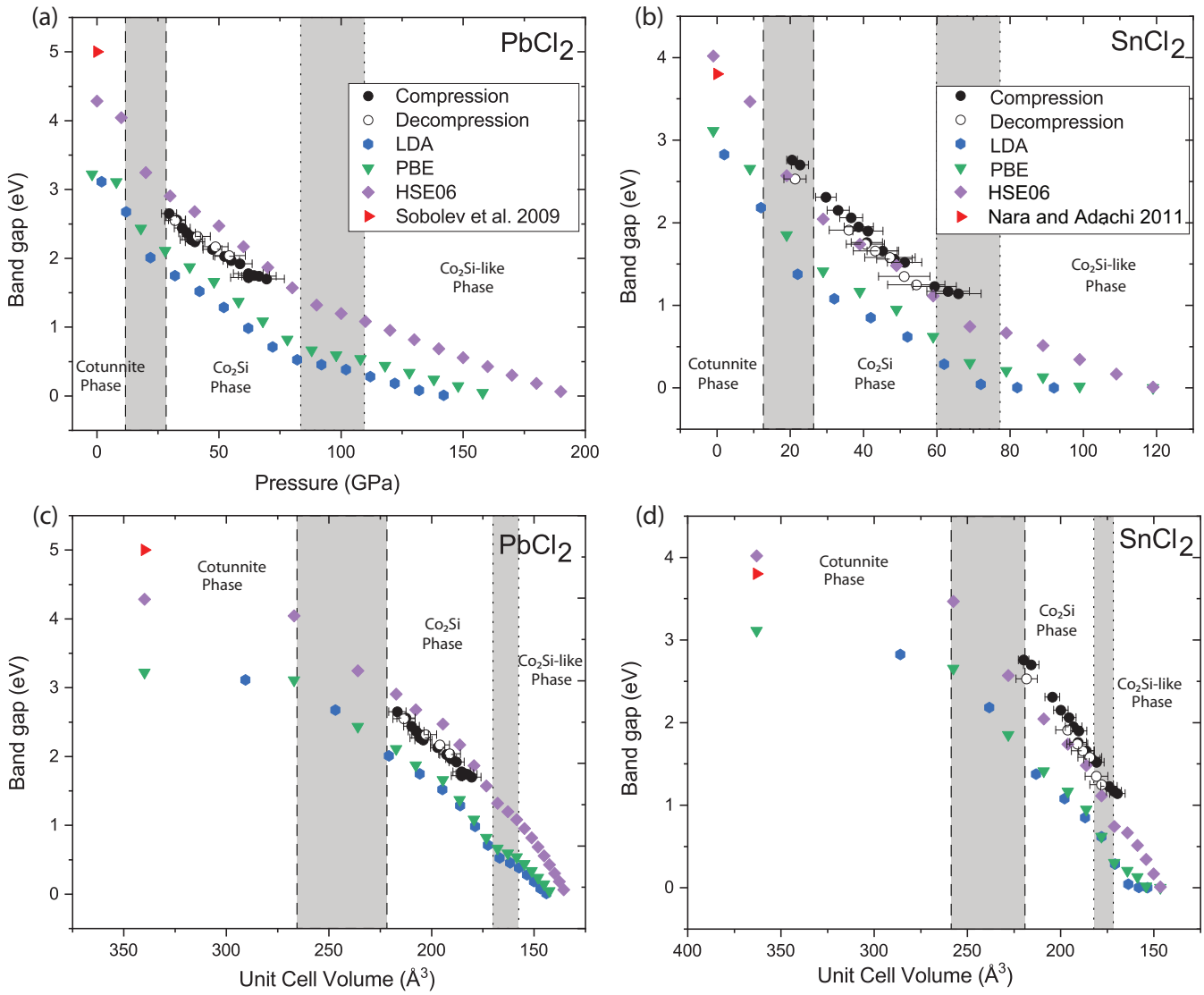


FIG. 5. Band gap as a function of pressure (top panels) and as a function of volume (bottom panels) from experiment and theory for $PbCl_2$ (left) and $SnCl_2$ (right). Zero-pressure band gaps were obtained from Sobolev *et al.* [55] for $PbCl_2$ and Nara and Adachi [56] for $SnCl_2$. The gray box with dashed lines shows the pressure range for the transition from the ninefold-coordinated cotunnite to the tenfold-coordinated $Co_2Si$ structure, and the gray box with dotted lines shows the pressure range for phase transformation from the $Co_2Si$ structure to the 11-fold–coordinated $Co_2Si$-like structure, as labeled in Figs. 2 and 3. For both $PbCl_2$ and $SnCl_2$, HSE06 fits the data better than either LDA or PBE, albeit with a small overestimation of band gap. (Top) Extrapolation of our experimental data yields band-gap closing pressures of $206 \pm 24$ GPa for $PbCl_2$ and $97 \pm 6$ GPa for $SnCl_2$, in reasonable agreement with theory (200 and 120 GPa, respectively). (Bottom) Volumes for the experimental points are calculated using the equations-of-state model from our compression data. Around 230 $Å^3$ the slope steepens, corresponding to the emergence of the $Co_2Si$ phase and the increase in coordination number in the crystal structure. Extrapolation of our experimental data to band-gap closure yields a closure volume of $131 \pm 21$ $Å^3$ for $PbCl_2$ and $150 \pm 5$ $Å^3$ in $SnCl_2$, in excellent agreement with theory (135 and 146 $Å^3$, respectively).

around 170 $Å^3$, and the $SnCl_2$ data show discontinuities corresponding to the expected phase boundaries in agreement with the calculated HSE06 results.

The observed steepening of band gap with unit-cell volume is likely due to the additive effects of compression and changes in interatomic geometry. Under compression, increased electron orbital overlap broadens the valence- and conduction bands, reducing band gaps. Interatomic geometry can further increase electronic orbital overlap as pressure-induced changes in crystal structures force neighboring orbitals into proximity of each other. Recent work shows the tunability of band gaps with cation-anion bond angles, finding that the band gap decreases as the crystal structure becomes more squarelike, in which electron orbitals are forced into overlapping configurations [57–59]. This is consistent with our observations on $PbCl_2$ and $SnCl_2$, in which we observe discontinuous down-shifts in the band gap across the transformation from cotunnite to the progressively more close-packed–like $Co_2Si$ and $Co_2Si$-like structures (Fig. 4).

Phrased another way, the increased shift in band gap with respect to volume at high compressions has a straightforward physical explanation: the approach to close packing of these materials as they progress through the two phase transitions, coupled with the concomitant increases in both cation and anion coordination, enhances the overlap between the cation conduction (mostly Pb $6p$ and Sn $5p$) and anion valence (mostly Cl $3p$) bonding states (see Appendix E, Fig. 11). For larger volumes (lower pressures) within the cotunnite structure, the inefficient packing of the anion framework within this quasipolymeric structure leads to a larger band gap; as the packing becomes more efficient, the rate of band-gap decrease is notably enhanced.

## IV. CONCLUSIONS

Static compression experiments to over 70 GPa and theoretical simulations to 200 GPa for $PbCl_2$ and 120 GPa for $SnCl_2$ show evidence of a continuous transition from the ninefold coordinated cotunnite structure to the tenfold coordinated $Co_2Si$ structure between 17 and 35 GPa in both $PbCl_2$ and $SnCl_2$. Upon further compression, density functionals predict the transition to an 11-fold–coordinated $Co_2Si$-like phase between 75 and 110 GPa in $PbCl_2$ and 60 and 80 GPa in $SnCl_2$, remaining the stable phase through the pressure range of our calculations.

Using equations of state validated by experiments, we calculate band-gap closure using the LDA, PBE, and HSE06 functionals. The hybrid functional HSE06 agrees best with our experimental data, confirming the superiority of HSE06 for calculating the electronic band structure of $AX_2$ compounds.

Our work shows the relationship between changing interatomic geometry and the closing of the band gap under high pressure, with applications for other $AX_2$ compounds in both fluid and solid states, which have been demonstrated to transition from low to high coordination number upon compression [7–19,22,23]. In particular, our results illustrate that the general pattern of phase transitions in $AX_2$ compounds from structures that can be viewed as polymeric to those characterized by close-packed anion packing recurs as cation coordination numbers increase under compression. In the particular case of cotunnite relative to the postcotunnite phases, a distorted but highly coordinated cation environment and complex prismatic anion coordination form a structure that can be viewed as composed of interlinked polymeric chains, which under compression converges on a phase that approaches close packing. Our band-gap measurements and calculations confirm that such a close-packed anion framework, coupled with high cation coordination numbers, is associated with the metallization of $AX_2$ oxides [14]. These results are of special interest for $SiO_2$, a major component of rocky planets that is predicted to exist in the cotunnite phase at pressures corresponding to super-Earth interiors [12]. Previous work investigating the band structure of $SiO_2$ at these conditions predicts metallization in the $I4/mmm$ phase near 1.4 TPa, though these calculations were performed using traditional density functionals, motivating the use of hybrid functionals like HSE06 to better constrain the high-pressure band structures [19]. Prediction of metallic $SiO_2$ could inform us of its potential to influence the dynamics and chemical partitioning in the deep cores of giant planets.

## ACKNOWLEDGMENTS

This work was supported by DOE/NNSA through the Center for Materials at Extreme Conditions (CMEC) consortium Grant No. DE-NA0004032. E.F.O'B. and Q.W. acknowledge support from Grant No. EAR- 1620423 and the Consortium for Materials Properties Research in Earth Sciences (COMPRES) under NSF Cooperative Agreement No. EAR 16–06856. E.O'B. also acknowledges that a portion of this work was performed under the auspices of the U.S. Department of Energy by Lawrence Livermore National Laboratory under Contract No. DE-AC52-07NA27344. The Advanced Light Source is supported by the Director, Office of Science, Office of Basic Energy Sciences, of the U.S. Department of Energy under Contract No. DE-AC02-05CH11231. S.S. was supported by Natural Environment Research Council (NERC) Grant No. NE/K006290/1. The calculations were performed on ARC1, ARC2, and ARC 3, part of the High-Performance Computing facilities at the University of Leeds, United Kingdom, and ARCHER, the United Kingdom's national high-performance computing service.

## APPENDIX A: X-RAY DIFFRACTION PATTERNS

X-ray diffraction patterns collected at the Advanced Light Source synchrotron.

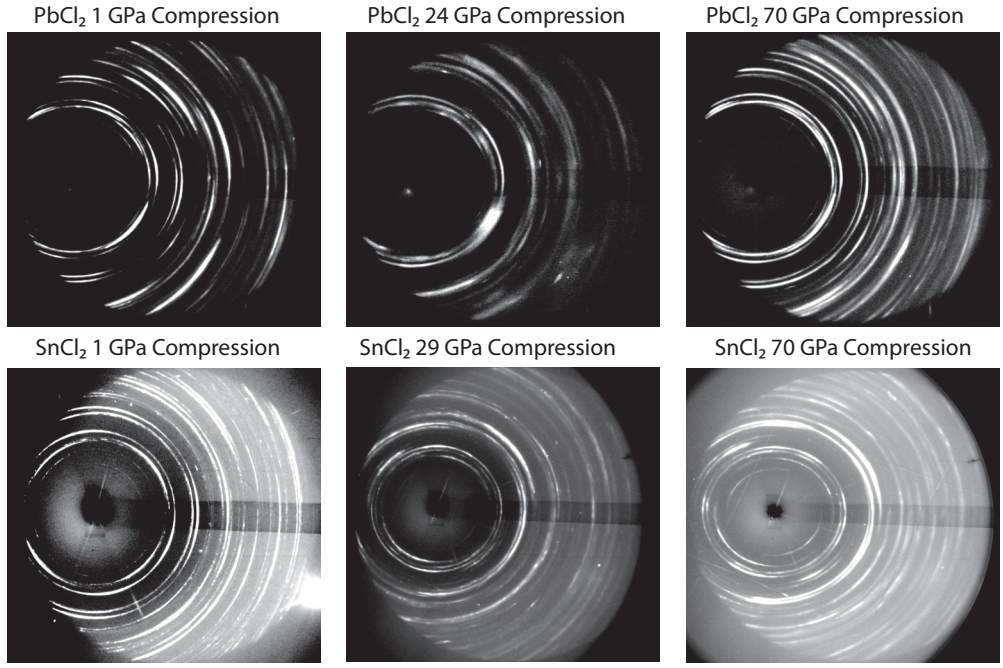


FIG. 6. Raw x-ray diffraction data for $PbCl_2$ (top) and $SnCl_2$ (bottom). Patterns for the cotunnite phase (left), transitional phase (middle), and $Co_2Si$ phase (right) are shown for each compound.

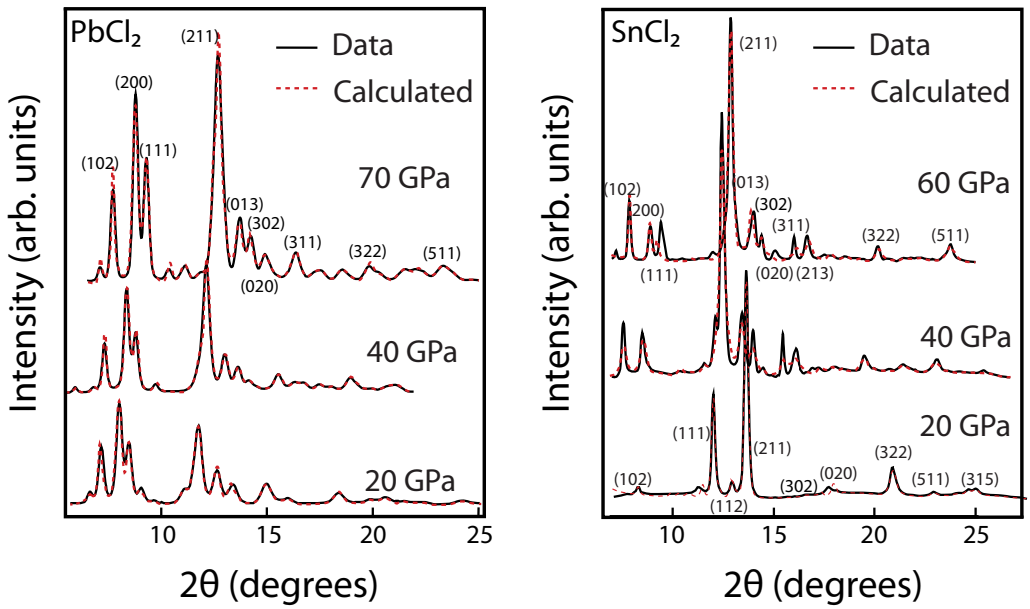


FIG. 7. X-ray diffraction patterns for $PbCl_2$ (left) and $SnCl_2$ (right). Both observed (black) and patterns calculated with Rietveld refinement (dashed red) are shown.

## APPENDIX B: FITS FOR EQUATIONS OF STATE

Weighted least-squares fits of the Eulerian strain vs normalized strain for the low pressure phase (f vs. F) and effective strain vs normalized strain high pressure phase (g vs. G).

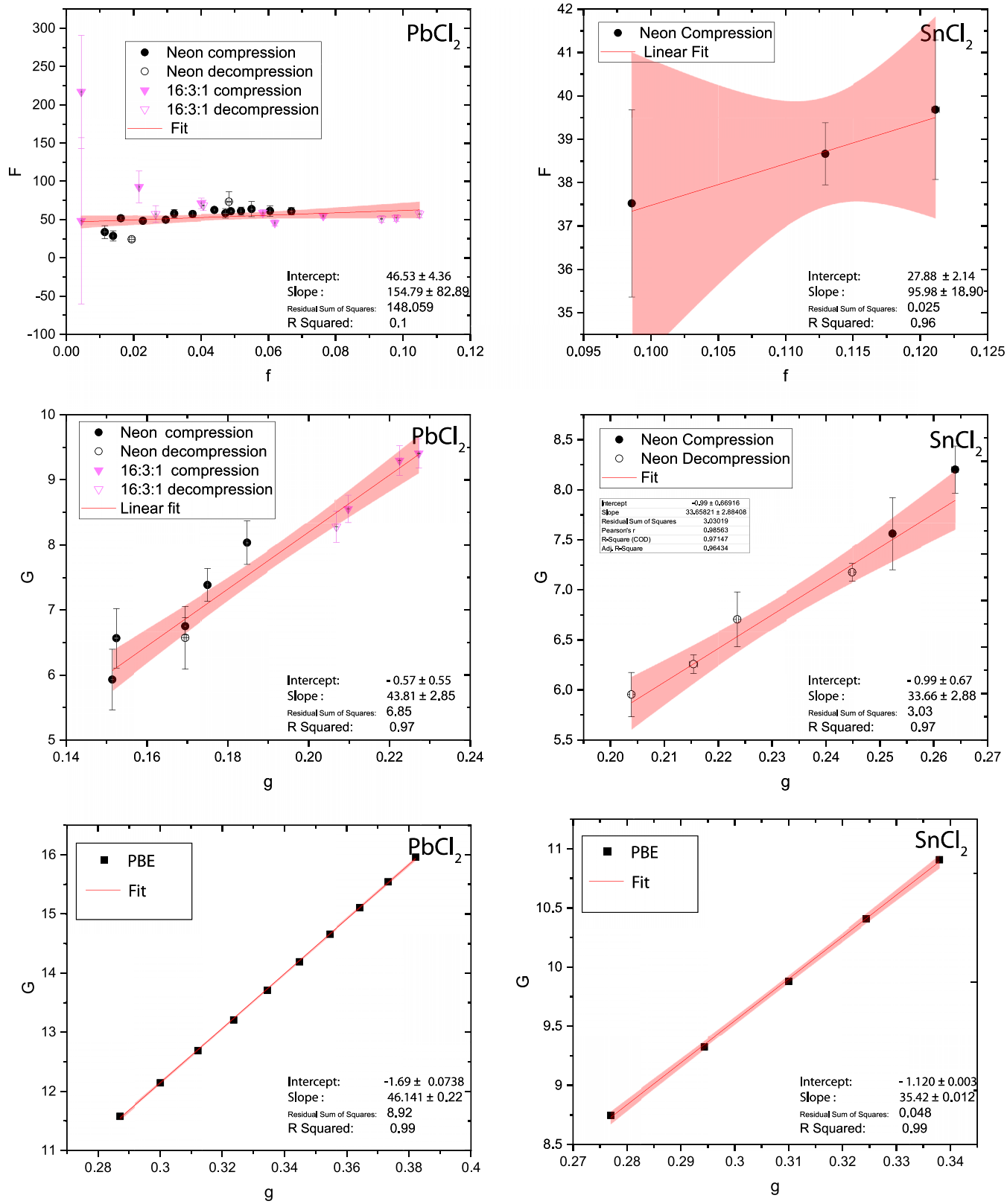


FIG. 8. Eulerian strain vs normalized strain ($F$ vs $f$) (cotunnite phase, top) and effective strain vs normalized strain ($G$ vs $g$) ($Co_2Si$ phase, middle and $Co_2Si$-like phase, bottom) are shown for $PbCl_2$ (left) and $SnCl_2$ (right). $F$ vs $f$ plots were used to determine the equations of state for the low-pressure phases, while $G$ vs $g$ was used for high-pressure phases [47]. Data from the phase-transition zone fit neither equation of state and were thus omitted. A weighted least-squares fit was applied to each dataset (red lines) and 95% confidence intervals are shown (red shading).

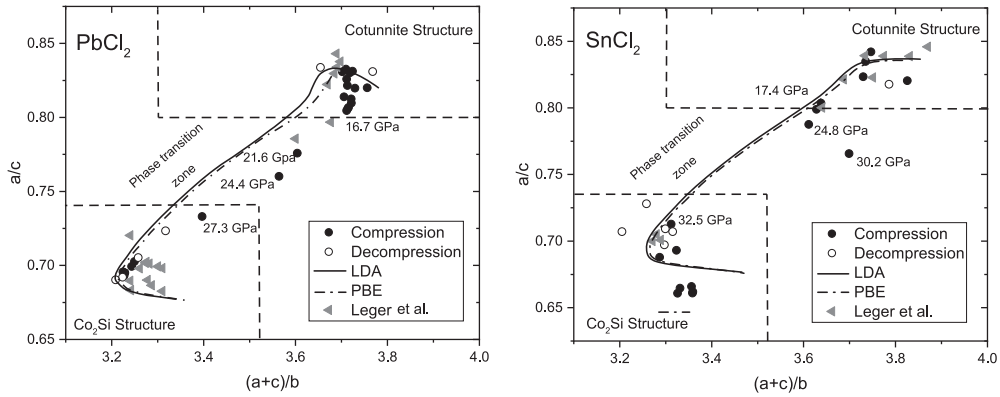


FIG. 9. Lattice parameter ratios of $PbCl_2$ (left) and $SnCl_2$ (right). Borders that define the phases follow Stan *et al.* [13]. Circles are data from this study, with solid circles indicating data taken on compression and empty circles those taken on decompression. Data from Leger *et al.* [10] are plotted as gray triangles. Calculated lattice ratios are shown as the solid (LDA) and dashed-dotted (PBE) curves.

## APPENDIX C: USING RATIOS OF THE LATTICE PARAMETERS TO DETERMINE PHASE CHANGES

The transformation between the cotunnite and $Co_2Si$ structures is characterized by a shift in the ratios of lattice parameters and a change in coordination from nine- to tenfold. Jeitschko [47] and Leger *et al.* [8] show that the $a/c$ and $(a+c)/b$ ratios distinguish between phases with orthorhombic (*Pnma*) symmetry. These ratios were later updated by Stan *et al.* [13], who show that for the cotunnite structure $a/c = 0.8$–$0.9$ and $(a+c)/b = 3.3$–$4.0$, and for $Co_2Si$ $a/c = 0.7$–$0.78$ and $(a+c)/b = 2.90$–$3.56$. When our data are plotted using these ratios, we see a clear distinction between the cotunnite and $Co_2Si$ phases (Fig. 9). Points that fall between the two phases are between 17 and 27 GPa for $PbCl_2$ and 17 and 33 GPa for $SnCl_2$. LDA and PBE calculations follow experimental data closely over the pressure range of our experiments. Here, the shift to the distorted $Co_2Si$-like phase is seen as a strong inflection point toward higher $(a+c)/b$ values near $(a+c)/b = 3.2$.

## APPENDIX D: ABSORPTION EDGE SPECTROSCOPY WITH PRESSURE

Examples of raw band-gap data collected using FTIR spectroscopy (Fig. 10), and all band gap data are shown (Table II).

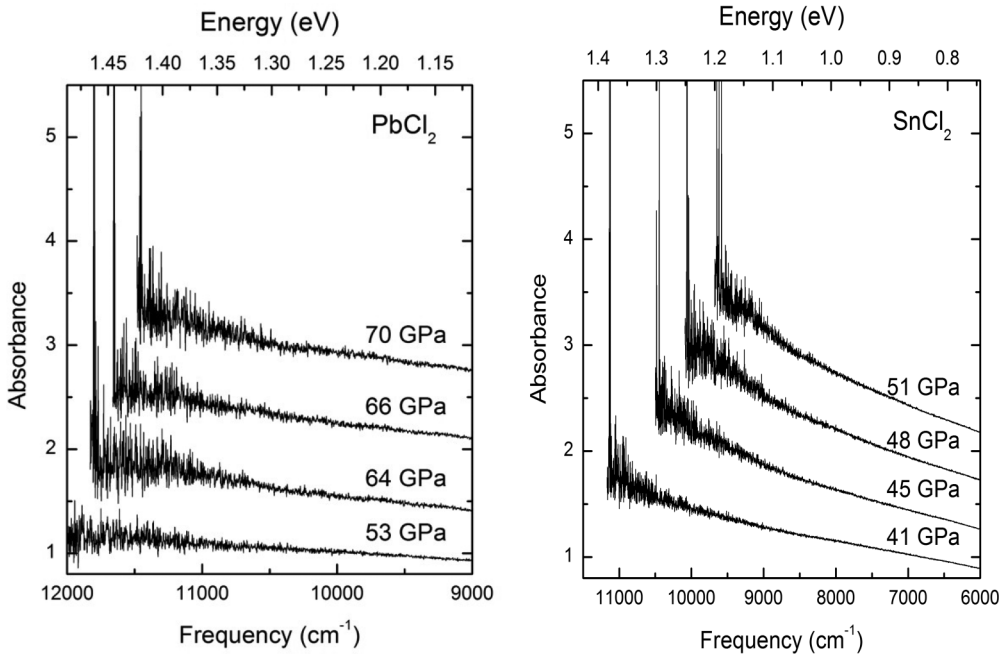


FIG. 10. Representative high-pressure spectra of the absorption edge of $PbCl_2$ (a) and $SnCl_2$ (b). No exciton peaks are resolved within these experiments. These spectra show that the energy of the band gap *decreases* as pressure *increases*. Spectra are stacked for clarity.

TABLE II. Absorption edge Experimental Data: Pressures, Unit Cell Volume, and Band gaps. Experimental data for absorption-edge measurements: Measured pressures and volumes are shown with their values in the first column and confidence bands in the second column. Pressures were determined using the standard ruby fluorescence technique, and volumes were determined using the experimentally determined equations of state. At larger band gaps (3.1–1.55 eV) the Horiba LabRam HR Evolution was used and at lower band gaps (1.74–1.05 eV) the Bruker Vertex 70v FTIR spectrometer was used. The Horiba detects the middle of the absorption edge, and the Bruker detects the very bottom of the absorption edge, introducing an instrument-induced discontinuity in the pressure-band gap and volume-band gap trends. The band gaps of the infrared data were adjusted by comparing the last visible-light measurement and first IR measurement (62 and 64.3 GPa for $PbCl_2$ and 38.7 and 40.9 GPa for $SnCl_2$) to make a correction assuming the band shape remains the same. This results in an upshift in the IR data of 0.3 eV in both compounds. Measured and adjusted band-gap values are shown.

| | Pressure (GPa) | | Volume (Å$^3$) | | Measured band gap (eV) | Adjusted band gap (eV) |
|---|---|---|---|---|---|---|
| $PbCl_2$ | 29.57 | 3.11 | 299.20 | 0.15 | 2.65 | – |
| | 32.78 | 3.5 | 292.50 | 0.10 | 2.56 | – |
| | 34.99 | 3.24 | 216.69 | 4.27 | 2.44 | – |
| | 36.9 | 3.4 | 212.48 | 4.41 | 2.37 | – |
| | 38.7 | 3.69 | 209.78 | 3.85 | 2.32 | – |
| | 40.16 | 3.97 | 207.57 | 3.86 | 2.24 | – |
| | 38.7 | 4.55 | 205.57 | 4.02 | 2.27 | – |
| | 47.3 | 3.81 | 204.0 | 4.19 | 2.13 | – |
| | 52.27 | 4.05 | 205.57 | 4.96 | 2.03 | – |
| | 55.07 | 3.36 | 197.04 | 3.46 | 1.97 | – |
| | 58.56 | 5.03 | 192.75 | 3.34 | 1.92 | – |
| | 62 | 7.2 | 190.50 | 2.64 | 1.72 | – |
| | 62 | 6.05 | 187.84 | 3.72 | 1.78 | – |
| | 64.3 | 6.33 | 185.37 | 5.05 | 1.45 | 1.75 |
| | 66.4 | 6.99 | 185.37 | 4.24 | 1.44 | 1.74 |
| | 69.5 | 7.25 | 183.79 | 4.28 | 1.40 | 1.7 |
| | 54.16 | 6.59 | 182.40 | 4.58 | 2.04 | – |
| | 48.55 | 5.21 | 180.42 | 4.53 | 2.17 | – |
| | 41.23 | 5.17 | 191.23 | 5.27 | 2.32 | – |
| | 32.02 | 4.22 | 195.92 | 4.62 | 2.55 | – |
| $SnCl_2$ | 20.48 | 1.45 | 219.86 | 2.79 | 2.75 | – |
| | 22.63 | 2.33 | 215.84 | 4.16 | 2.72 | – |
| | 29.72 | 2.81 | 204.48 | 3.99 | 2.34 | – |
| | 33.08 | 3.01 | 199.89 | 3.89 | 2.18 | – |
| | 36.61 | 3.12 | 195.49 | 3.68 | 2.06 | – |
| | 38.68 | 3.98 | 193.1 | 4.47 | 1.95 | 1.9 |
| | 41.2 | 4.12 | 190.33 | 4.36 | 1.6 | 1.76 |
| | 40.9 | 4.27 | 190.65 | 4.55 | 1.46 | 1.66 |
| | 45.24 | 4.3 | 186.21 | 4.16 | 1.36 | 1.56 |
| | 48.4 | 4.85 | 183.23 | 4.4 | 1.26 | 1.52 |
| | 51.2 | 4.71 | 180.74 | 4.04 | 1.22 | 1.23 |
| | 59.4 | 5.93 | 174.17 | 4.39 | 0.93 | 1.17 |
| | 63.1 | 5.81 | 171.49 | 4.04 | 0.87 | 1.14 |
| | 65.9 | 6.21 | 169.58 | 4.13 | 0.84 | 1.25 |
| | 54.4 | 7.82 | 178.061 | 6.34 | 0.95 | 1.35 |
| | 51.1 | 7.01 | 180.83 | 6.04 | 1.05 | 1.58 |
| | 47.2 | 6.87 | 184.34 | 6.4 | 1.28 | 1.66 |
| | 43.2 | 5.99 | 188.24 | 6.08 | 1.36 | 1.74 |
| | 40.5 | 5.21 | 191.08 | 5.61 | 1.44 | – |
| | 36 | 5.4 | 196.23 | 6.5 | 1.91 | – |
| | 21.3 | 3.02 | 218.29 | 5.67 | 2.53 | |

## APPENDIX E: DENSITY OF STATES CALCULATIONS

The partial density of states for $PbCl_2$ and $SnCl_2$ calculated using the HSE06 exchange-correlation functional shows that the valence band has primarily Cl 3*p* and Pb, Sn 6*s* character. The unoccupied conduction band has mainly Pb, Sn 6*p* and diminished Cl 3*p* character. All bands broaden with increasing pressure, as band gap reduces from about 4 eV at ambient pressure in each $PbCl_2$ and $SnCl_2$ to closure.

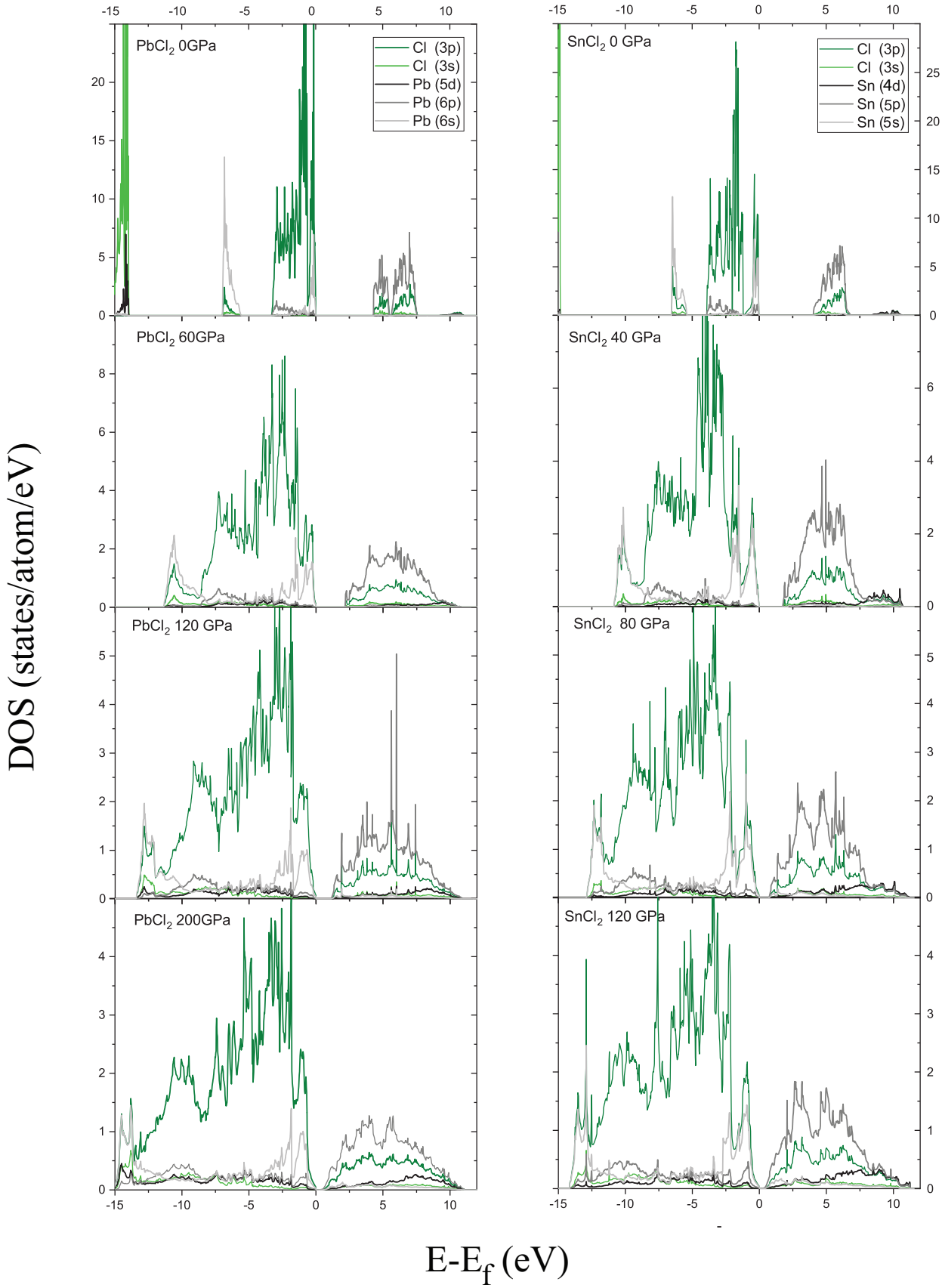


FIG. 11. Calculated density of states (DOS) for $PbCl_2$ at 0, 60, 120, and 200 GPa (left) and $SnCl_2$ at 0, 40, 80, and 120 GPa (right) using HSE06 density functional. Ambient-pressure DOS (top panels) show a clear distinction between *s* and *p* orbitals in Pb, Sn, and Cl, with an energy gap of around 4 eV. We observe a broadening of all states to higher pressure (downward panels).

## APPENDIX F: EXPERIMENTAL DATA

The full data set acquired from x-ray diffraction is shown (Table III).

TABLE III. Experimental Data: Pressures, Unit Cell Volume, and Lattice parameters. Experimental data: Measured pressures, volumes, and lattice parameters for $SnCl_2$ and $PbCl_2$ on compression and decompression. The determined value for each measured parameter is shown in the first column, and the confidence band is shown in the second column. Volumes and lattice parameters were obtained though Rietveld refinement of our x-ray diffraction data. At each pressure step we measured pressure in several locations determined using the standard ruby fluorescence technique [27]. Pressures reported are the median pressure, and the error bars represent the total range of deviation from median pressure for a given pressure step.

| | Pressure (GPa) | | Volume (Å$^3$) | | $a$(Å) | | $b$(Å) | | $c$(Å) | |
|---|---|---|---|---|---|---|---|---|---|---|
| $PbCl_2$ | 1.6 | 0.2 | 299.20 | 0.15 | 7.556 | 0.001 | 4.412 | 0.001 | 8.973 | 0.005 |
| | 8.3 | 2.6 | 292.50 | 0.10 | 7.459 | 0.002 | 7.000 | 0.004 | 8.935 | 0.004 |
| | 10.8 | 2.3 | 286.85 | 0.15 | 7.358 | 0.002 | 4.369 | 0.005 | 8.937 | 0.006 |
| | 14.6 | 2.6 | 277.10 | 0.13 | 7.319 | 0.002 | 4.244 | 0.004 | 8.920 | 0.005 |
| | 17.4 | 3.0 | 242.80 | 0.10 | 6.813 | 0.011 | 4.203 | 0.006 | 8.478 | 0.002 |
| | 21.8 | 2.4 | 234.31 | 0.10 | 6.707 | 0.001 | 4.162 | 0.001 | 8.394 | 0.001 |
| | 24.8 | 3.0 | 229.70 | 0.15 | 6.602 | 0.001 | 4.150 | 0.001 | 8.383 | 0.002 |
| | 30.3 | 4.0 | 215.33 | 0.10 | 6.419 | 0.001 | 4.002 | 0.002 | 8.383 | 0.003 |
| | 32.6 | 4.6 | 201.92 | 0.10 | 5.709 | 0.002 | 4.262 | 0.001 | 8.300 | 0.000 |
| | 36.1 | 0.3 | 203.70 | 0.10 | 5.770 | 0.002 | 4.241 | 0.001 | 8.325 | 0.003 |
| | 41.0 | 2.6 | 195.60 | 0.10 | 5.770 | 0.004 | 4.187 | 0.002 | 8.096 | 0.004 |
| | 45.1 | 2.0 | 181.70 | 0.13 | 5.455 | 0.004 | 4.066 | 0.004 | 8.191 | 0.004 |
| | 51.7 | 1.6 | 176.99 | 0.04 | 5.392 | 0.002 | 4.030 | 0.003 | 8.145 | 0.002 |
| | 57.0 | 1.4 | 174.82 | 0.05 | 5.365 | 0.002 | 4.015 | 0.004 | 8.117 | 0.003 |
| | 63.0 | 3.0 | 172.32 | 0.06 | 5.321 | 0.002 | 4.021 | 0.004 | 8.053 | 0.003 |
| | 71.0 | 2.0 | 168.40 | 0.20 | 5.300 | 0.006 | 3.984 | 0.007 | 7.973 | 0.007 |
| | 67.1 | 1.8 | 176.70 | 0.10 | 5.556 | 0.005 | 4.047 | 0.003 | 7.859 | 0.003 |
| | 58.3 | 0.7 | 174.92 | 0.10 | 5.486 | 0.002 | 4.051 | 0.000 | 7.870 | 0.000 |
| | 50.7 | 2.1 | 182.70 | 0.02 | 5.618 | 0.001 | 4.104 | 0.001 | 7.923 | 0.002 |
| | 46.0 | 0.6 | 185.82 | 0.30 | 5.770 | 0.005 | 4.203 | 0.007 | 7.926 | 0.005 |
| | 42.0 | 1.6 | 190.40 | 0.11 | 5.632 | 0.005 | 4.243 | 0.004 | 7.966 | 0.004 |
| $SnCl_2$ | 1.6 | 0.2 | 299.20 | 0.15 | 7.556 | 0.001 | 4.412 | 0.001 | 8.973 | 0.005 |
| | 8.3 | 2.6 | 292.50 | 0.10 | 7.459 | 0.002 | 7.000 | 0.004 | 8.935 | 0.004 |
| | 10.8 | 2.3 | 286.85 | 0.15 | 7.358 | 0.002 | 4.369 | 0.005 | 8.937 | 0.006 |
| | 14.6 | 2.6 | 277.10 | 0.13 | 7.319 | 0.002 | 4.244 | 0.004 | 8.920 | 0.005 |
| | 17.4 | 3.0 | 242.80 | 0.10 | 6.813 | 0.011 | 4.203 | 0.006 | 8.478 | 0.002 |
| | 21.8 | 2.4 | 234.31 | 0.10 | 6.707 | 0.001 | 4.162 | 0.001 | 8.394 | 0.001 |
| | 24.8 | 3.0 | 229.70 | 0.15 | 6.602 | 0.001 | 4.150 | 0.001 | 8.383 | 0.002 |
| | 30.3 | 4.0 | 215.33 | 0.10 | 6.419 | 0.001 | 4.002 | 0.002 | 8.383 | 0.003 |
| | 32.6 | 2.6 | 201.92 | 0.10 | 5.709 | 0.002 | 4.262 | 0.001 | 8.300 | 0.000 |
| | 36.1 | 0.3 | 203.70 | 0.10 | 5.770 | 0.002 | 4.241 | 0.001 | 8.325 | 0.003 |
| | 41.0 | 2.6 | 195.60 | 0.10 | 5.770 | 0.004 | 4.187 | 0.002 | 8.096 | 0.004 |
| | 45.1 | 2.0 | 181.70 | 0.13 | 5.455 | 0.004 | 4.066 | 0.004 | 8.191 | 0.004 |
| | 51.7 | 1.6 | 176.99 | 0.04 | 5.392 | 0.002 | 4.030 | 0.003 | 8.145 | 0.002 |
| | 57.0 | 1.4 | 174.82 | 0.05 | 5.365 | 0.002 | 4.015 | 0.004 | 8.117 | 0.003 |
| | 63.0 | 3.0 | 172.32 | 0.06 | 5.321 | 0.002 | 4.021 | 0.004 | 8.053 | 0.003 |
| | 71.0 | 2.0 | 168.40 | 0.20 | 5.300 | 0.006 | 3.984 | 0.007 | 7.973 | 0.007 |
| | 67.1 | 1.8 | 176.70 | 0.10 | 5.556 | 0.005 | 4.047 | 0.003 | 7.859 | 0.003 |
| | 58.3 | 0.7 | 174.92 | 0.10 | 5.486 | 0.002 | 4.051 | 0.000 | 7.870 | 0.000 |
| | 50.7 | 2.1 | 182.70 | 0.02 | 5.618 | 0.001 | 4.104 | 0.001 | 7.923 | 0.002 |
| | 46.0 | 0.6 | 185.82 | 0.30 | 5.770 | 0.005 | 4.203 | 0.007 | 7.926 | 0.005 |
| | 42.0 | 1.6 | 190.40 | 0.11 | 5.632 | 0.005 | 4.243 | 0.004 | 7.966 | 0.004 |
| | 0.0 | 0.0 | 318.03 | 0.05 | 7.623 | 0.002 | 4.476 | 0.003 | 9.322 | 0.006 |

[1] N. F. Mott, *Metal-Insulator Transitions* (CRC Press, London, 1990).

[2] D. A. Young, *Phase Diagrams of the Elements* (University of California Press, Berkeley, 1991).

[3] C. J. Pickard, I. Errea, and M. I. Eremets,, Annu. Rev. Condens. Matter Phys. **11**, 57 (2020).

[4] L. Stixrude and R. Jeanloz, Proc. Natl. Acad. Sci. USA **105**, 11071 (2008).

[5] P. M. Celliers, P. Loubeyre, J. H. Eggert, S. Brygoo, R. S. McWilliams, D. G. Hicks, T. R. Boehly, R. Jeanloz, and G. W. Collins, Phys. Rev. Lett. **104**, 184503 (2010).

[6] L. Pauling, *The Nature of the Chemical Bond*, 3rd ed. (Cornell University Press, Ithaca, NY, 1960).

[7] J. M. Leger, J. Haines, and A. Atouf, J. Appl. Crystallogr. **28**, 416 (1995).

[8] J. M. Leger, J. Haines, A. Atouf, O. Schulte, and S. Hull, Phys. Rev. B **52**, 13247 (1995).

[9] J. M. Leger, J. Haines, and A. Atouf, Phys. Rev. B **51**, 3902 (1995).

[10] J. M. Leger, J. Haines, and A. Atouf, J. Phys. Chem. Solids **57**, 7 (1996).

[11] J. Haines, J. M. Leger, and O. Schulte, J. Phys.: Condens. Matter **8**, 1631 (1996).

[12] A. R. Oganov, M. J. Gillan, and G. D. Price, Phys. Rev. B **71**, 064104 (2005).

[13] C. V. Stan, R. Dutta, C. E. White, V. Prakapenka, and T. S. Duffy, Phys. Rev. B **94**, 024104 (2016).

[14] M. J. Lyle, C. J. Pickard, and R. J. Needs, Proc. Natl. Acad. Sci. USA **112**, 6898 (2015).

[15] O. Ohtaka, D. Andrault, P. Bouvier, E. Schultz, and M. Mezouar, J. Appl. Crystallogr. **38**, 727 (2005).

[16] S. R. Shieh, A. Kubo, T. S. Duffy, V. B. Prakapenka, and G. Shen, Phys. Rev. B **73**, 014105 (2006).

[17] S. J. Duclos, Y. K. Vohra, A. L. Ruoff, A. Jayaraman, and G. P. Espinosa, Phys. Rev. B **38**, 7755 (1988).

[18] H. X. Song, L. Liu, H. Y. Geng, and Q. Wu, Phys. Rev. B **87**, 184103 (2013).

[19] S. Duwal, C. A. McCoy, P. F. Weck, P. Kalita, H. L. Hanshaw, K. Cochrane, T. Ao, and S. Root, Phys. Rev. B **102**, 024105 (2020).

[20] M. Millot, N. Dubrovinskaia, A. Cernok, S. Blaha, L. Dubrovinsky, D. G. Braun, P. M. Celliers, G. W. Collins, J. H. Eggert, and R. Jeanloz, Science **347**, 418 (2015).

[21] H. Shu, Y. Zhang, B. Wang, H. Dong, T. Tobase, J. Ye, X. Huang, S. Fu, and T. Sekine, Phys. Plasmas **27**, 030701 (2020).

[22] B. Kalkan, B. Godwal, S. V. Raju, and R. Jeanloz, Sci. Rep. **8**, 6844 (2018).

[23] A. Denoeud, S. Mazevet, F. Guyot, F. Dorchies, J. Gaudin, A. Ravasio, E. Brambrink, and A. Benuzzi-Mounaix, Phys. Rev. E **94**, 031201(R) (2016).

[24] E. M. Stolper and T. J. Ahrens, Geophys. Res. Lett. **14**, 1231 (1987).

[25] P. J. Hasnip, K. Refson, M. I. J. Probert, J. R. Yates, S. J. Clark, and C. J. Pickard, Philos. Trans. R. Soc., A **372**, 20130270 (2014).

[26] J. P. Perdew and M. Levy, Phys. Rev. Lett. **51**, 1884 (1983).

[27] A. Dewaele, M. Torrent, P. Loubeyre, and M. Mezouar, Phys. Rev. B **78**, 104102 (2008).

[28] M. H. Kuok and L. H. Lim, J. Raman Spectrosc. **21**, 675 (1990).

[29] C. Carabatos-Nedelec, F. Brehat, and B. Wyncke, Infrared Phys. **31**, 611 (1991).

[30] Q. Williams and R. Jeanloz, Phys. Rev. Lett. **56**, 163 (1986).

[31] A. P. Hammersley, S. O. Svensson, M. Hanfland, A. N. Fitch, and D. Hausermann, High Pressure Res. **14**, 235 (1996).

[32] C. Prescher and V. B. Prakapenka, High Pressure Res. **35**, 223 (2015).

[33] A. C. Larson and R.B. Von Dreele, Los Alamos National Laboratory Report LAUR 86–748 (2004).

[34] G. Kresse and J. Furthmuller, Comput. Mater. Sci. **6**, 15 (1996).

[35] G. Kresse and J. Furthmuller, Phys. Rev. B **54**, 11169 (1996).

[36] P. E. Blochl, Phys. Rev. B **50**, 17953 (1994).

[37] G. Kresse and D. Joubert, Phys. Rev. B **59**, 1758 (1999).

[38] J. P. Perdew and A. Zunger, Phys. Rev. B **23**, 5048 (1981).

[39] J. P. Perdew, K. Burke, and M. Ernzerhof, Phys. Rev. Lett. **77**, 3865 (1996).

[40] H. Xiao, J. Tahir-Kheli, and W. A. Goddard, J. Phys. Chem. Lett. **2**, 212 (2011).

[41] A. V. Krukau, O. A. Vydrov, A. F. Izmaylov, and G. E. Scuseria, J. Chem. Phys. **125**, 224106 (2006).

[42] A. J. Garza and G. E. Scuseria, J. Phys. Chem. Lett. **7**, 4165 (2016).

[43] H. J. Monkhorst and J. D. Pack, Phys. Rev. B **13**, 5188 (1976).

[44] A. R. Oganov, J. P. Brodholt, and G. D. Price, Earth Planet. Sci. Lett. **184**, 555 (2001).

[45] B. K. Godwal, S. Stackhouse, J. Yan, S. Speziale, B. Militzer, and R. Jeanloz, Phys. Rev. B **87**, 100101(R) (2013).

[46] B. G. Hyde, M. O'Keeffe, W. M. Lyttle, and N. E. Brese, Acta Chem. Scand. **46**, 216 (1992).

[47] W. Jeitschko, Acta Crystallogr., Sect. B **24**, 930 (1968).

[48] I. Abrahams and D. Z. Demetriou, J. Solid State Chem. **149**, 28 (2000).

[49] R. Jeanloz, J. Geophys. Res. **94**, 5873 (1989).

[50] K. Momma and F. Izumi, J. Appl. Crystallogr. **44**, 1272 (2011).

[51] S. Froyen and M. L. Cohen, J. Phys. C **19**, 2623 (1986).

[52] P. Cervantes, Q. Williams, M. Cote, M. Rohlfing, M. L. Cohen, and S. G. Louie, Phys. Rev. B **58**, 9793 (1998).

[53] N. E. Christensen, A. Svane, and E. L. Peltzer y Blancá, Phys. Rev. B **72**, 014109 (2005).

[54] J.-M. Raulot, G. Baldinozzi, R. Seshadri, and P. Cortona, Solid State Sci. **4**, 467 (2002).

[55] V. V. Sobolev, A. I. Kalugin, and I. V. Vostrikov, J. Surf. Invest.: X-Ray, Synchrotron Neutron Tech. **3**, 48 (2009).

[56] J. Nara and S. Adachi, J. Appl. Phys. **109**, 083539 (2011).

[57] L. Zhang, K. Wang, and B. Zou, J. Phys. Chem. Lett. **11**, 4693 (2020).

[58] R. K. Hona and F. Ramezanipour, J. Chem. Sci. **131**, 12039 (2019).

[59] M. R. Filip, G. E. Eperon, H. J. Snaith, and F. Guistino, Nat. Commun. **5**, 5757 (2014).